

pubs.acs.org/cm Article

Thermal Atomic Layer Etching of Gold Using Sulfuryl Chloride for Chlorination and Triethylphosphine for Ligand Addition

Jonathan L. Partridge, Jessica A. Murdzek, Virginia L. Johnson, Andrew S. Cavanagh, Sandeep Sharma, and Steven M. George*



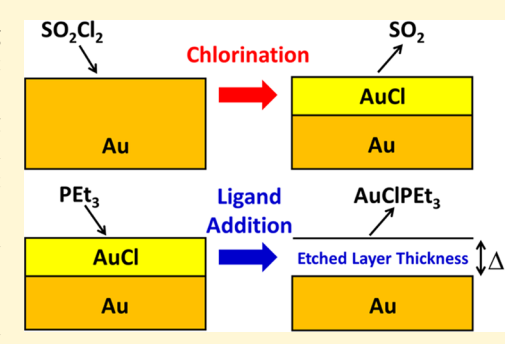
Cite This: Chem. Mater. 2024, 36, 5149-5159



ACCESS

Metrics & More

ABSTRACT: Thermal atomic layer etching (ALE) of gold was achieved using sequential chlorination and ligand-addition reactions. This two-step process first chlorinated gold using sulfuryl chloride (SO_2Cl_2) to form gold chloride. Subsequently, ligand addition to the gold chloride was performed using triethylphosphine (PEt₃) to yield a volatile gold etch product. Quartz crystal microbalance measurements on cubic crystalline gold films showed etching at temperatures from 75 to 175 °C. The most consistent etch rate was 0.44 ± 0.16 Å/cycle at 150 °C. A mass increase was observed during each SO_2Cl_2 exposure when forming the gold chloride. A mass loss was then monitored during each PEt₃ dose when ligand addition yielded a volatile etch product. In situ quadrupole mass spectrometry (QMS) studies on Au nanopowder at 150 °C showed the production of AuClPEt₃ as the dominant Au-containing etch product during PEt₃ exposures.



Article Recommendations

Time-dependent QMS studies also observed the AuClPEt₃⁺ ion intensity peaking at the beginning of each PEt₃ exposure. The AuClPEt₃⁺ ion intensity then decreased as the PEt₃⁺ ion intensity remained constant. This behavior indicates a self-limiting ligand-addition reaction. X-ray photoelectron spectroscopy on these Au nanopowders showed evidence for AuClPEt₃ on the surface of the Au nanopowder when the final exposure was PEt₃. Transmission electron microscopy analysis revealed that Au ALE did not roughen the crystalline Au nanoparticles. Powder X-ray diffraction measurements also showed narrower diffraction peaks after Au ALE on Au nanoparticles that were consistent with larger Au nanoparticles. This sintering effect may be caused by Au redistribution resulting from the disproportionation of the AuCl surface species. Using the same alternating exposures of SO₂Cl₂ and PEt₃, Cu and Ni nanopowders were also etched at 150 °C. Cu formed a volatile Cu₂Cl₂(PEt₃)₂ dimer during PEt₃ exposures at 150 °C. Likewise, Ni formed volatile NiCl₂(PEt₃)₂ during PEt₃ exposures at 150 °C. Gibbs free energy changes from ab inito calculations support these etch product observations and offer a thermodynamic explanation for the formation of a copper dimer. These studies illustrate that sequential chlorination and ligand-addition reactions can provide a useful ALE pathway for gold and other metals.

I. INTRODUCTION

Atomic layer etching (ALE) is a highly controllable etch process that utilizes two sequential, self-limiting surface reactions. The first reaction is a surface modification process. The second reaction then releases volatile species from the modified surface layer. ALE can be performed using either plasma or thermal methods. Plasma ALE involves energetic species that remove the modified surface layer. In contrast, thermal ALE uses thermal reactions to remove the modified surface layer.

A number of thermal ALE pathways have been developed in recent years. The first reported thermal ALE mechanism involved fluorination followed by ligand exchange. In this mechanism, fluorination is the surface modification step. Ligand exchange is then used to form a volatile etch product. This mechanism has been used to etch a variety of metal oxides, including Al_2O_3 , 5,6,10,11 ZrO_2 , 11,12 and HfO_2 . $^{11-13}$

Another thermal ALE mechanism is conversion, followed by volatile release of the converted layer. 3,14 In the conversion mechanism, the metal oxide is first converted to a different metal oxide that has a volatile fluoride. The conversion layer is then spontaneously etched by a thermal fluorination reaction. An example of this mechanism is WO₃ ALE. 14 The surface of WO₃ is converted to a B₂O₃ layer by BCl₃. HF then spontaneously removes the B₂O₃ layer. 14,15 Similar conversion mechanisms are also available for nitrides, such as TiN, where the nitride surface is oxidized to form TiO₂. 16 HF can then

Received: February 21, 2024 Revised: April 16, 2024 Accepted: April 25, 2024 Published: May 13, 2024





spontaneously etch the ${\rm TiO_2}$ surface layer by forming a volatile fluoride. 16,17

Conversion mechanisms can also be used to convert one metal oxide into another metal oxide that can undergo subsequent fluorination and ligand-exchange reactions. Examples of this mechanism include ZnO and SiO $_2$ ALE. 19,20 In these conversion reactions, trimethylaluminum (TMA) converts the surface to an ${\rm Al}_2{\rm O}_3$ layer. 19,20 The ${\rm Al}_2{\rm O}_3$ layer can then be removed by fluorination and ligand exchange. 10 This method can be extended to Si, SiGe, and Si $_3{\rm N}_4$ ALE by adding an initial oxidation reaction. $^{21-23}$

Elemental metals can also be etched by thermal ALE. These methods typically involve changing the oxidation number of the metal with oxygen or chloride reactants. $^{14,24-27}$ The resulting metal oxide or metal chloride can then be removed by ligand-substitution or ligand-addition reactions. $^{24-27}$ For example, Cu can be etched by first oxidizing the Cu surface to form a copper oxide layer. The copper oxide layer can then be removed by a ligand-substitution and hydrogen-transfer reaction with Hhfac to form volatile $\text{Cu}(\text{hfac})_2$ and H_2O . 26

The thermal ALE of Ni was also demonstrated recently using SO_2Cl_2 to chlorinate the Ni surface to form $NiCl_2$. Exposure to PMe₃ then resulted in ligand addition with $NiCl_2$ to form volatile $NiCl_2(PMe_3)_2$ etch products. In related work, a variety of group 10 metal chlorides, including $NiCl_2$, $PdCl_2$, and $PtCl_2$, were spontaneously etched by ligand addition with PMe_3 to form $NiCl_2(PMe_3)_2$, $PdCl_2(PMe_3)_2$, and $PtCl_2(PMe_3)_2$ volatile products.

Co ALE was also reported using SO_2Cl_2 to chlorinate the Co surface to form $CoCl_2$. Exposure to tetramethylethylenediamine (TMEDA) then led to the formation of volatile $CoCl_2(TMEDA)$ etch products. The first-row metal oxides Fe_2O_3 , CoO, NiO, and ZnO were also shown to undergo a similar chlorination and ligand-addition reaction using SO_2Cl_2 for chlorination and TMEDA for ligand addition. These sequential reactions formed volatile $MCl_2(TMEDA)$ species.

Gold is one of the most revered and valuable metals. Au is used for interconnects, photocatalysts, and microelectromechanical devices. ^{31–34} Au also has important applications in photonics, chemical and biological sensing, and plasmonics. ^{35–37} Despite the need for controlled Au film thickness, there are only a few known Au atomic layer deposition (ALD) processes. Two plasma Au ALD processes utilize either hydrogen or oxygen plasmas. One thermal Au ALD process employs alternating Me₂Au(S₂CNEt₂) and O₃ reactants, where O₃ is used to combust the ligands of the Au precursor. ⁴⁰ A second thermal Au ALD process alternates between AuClPEt₃ as the Au-containing precursor and (Me₃Ge)₂DHP as a reducing agent. ⁴¹ Another work shows that a variety of volatile Au(I) precursors can be synthesized, with Au ALD demonstrated using alternating Au(N(SiMe₃)₂)-(PEt₃) as the Au-containing precursor and BH₃(NHMe₂) as a reducing agent. ⁴²

In comparison to the few demonstrated Au ALD processes, there are no reported thermal ALE processes. A thermal Au ALE process could be used in conjunction with Au ALD to obtain Au films with precise thicknesses control on 3D structures. Metal ALD typically suffers from poor nucleation on oxide surfaces. ^{43,44} These nucleation difficulties lead to island growth and initial surface roughness for ultrathin films. ⁴⁴ One solution is to overgrow the metal film and then etch back to obtain a continuous and smooth ultrathin film. ⁴⁵ This deposit and etchback approach was recently illustrated using

alternating Al_2O_3 ALD and thermal Al_2O_3 ALE to enhance the yield of MIM capacitors using ultrathin Al_2O_3 insulating layers.⁴⁵

In this work, Au thermal ALE was demonstrated using the sequential reaction sequence shown in Figure 1. SO₂Cl₂ was

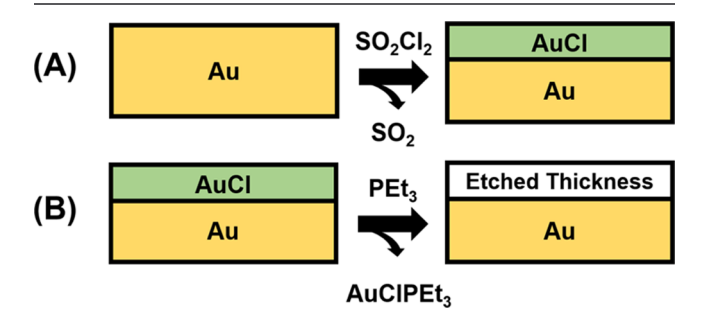


Figure 1. Proposed mechanism for Au ALE using SO_2Cl_2 for chlorination and PEt_3 for ligand addition.

employed as a chlorination reactant to form AuCl. Triethylphosphine (PEt₃) was then utilized as a ligand-addition reactant to remove the AuCl and form AuClPEt₃ as the volatile product. This sequential reaction sequence was also shown to be successful for etching Ni and Cu. These new results demonstrate that chlorination and ligand addition is an important mechanism for metal ALE. Many new applications for metal ALE are expected based on chlorination and ligand-addition reactions.

II. EXPERIMENTAL SECTION

II.I. X-ray Diffraction (XRD) Studies. Grazing incidence X-ray diffraction (GI-XRD) was performed on the gold film on the gold-coated quartz crystal used for the QCM studies prior to the ALE experiments. The GI-XRD scans were performed using a Bede D1 from Bruker with radiation from Cu K α (λ = 1.540 Å). The X-ray tube filament voltage was 40 kV, and the current was 35 mA. The incident angle used for GI-XRD was 0.8°.

Powder X-ray diffraction (PXRD) was also performed on Au nanopowder samples used for the QMS studies before and after Au ALE. A Bruker AXS D8 Advance A25 with Cu K α radiation was used for these studies. The X-ray tube filament voltage was 40 kV, and the current was 40 mA. 2θ scans were performed from 30 to 90° with a step size of $0.0275^{\circ}/\text{step}$ and a scan speed of 1 s/step. Particle size analysis using the Sherrer equation was performed using the full width at half-maximum of the diffraction peaks.

II.II. Quartz Crystal Microbalance (QCM) Studies. The QCM experiments were performed in a viscous flow reactor. ⁴⁶ The reaction temperatures were maintained by a proportional-integral-derivative temperature controller (2604, Eurotherm). A constant flow of ultrahigh purity Ar gas was employed as the carrier and purge gas using mass flow controllers (Type 1179A, MKS). A mechanical pump (Pascal 2015SD, Alcatel) was attached at the back of the reactor. The reactor pressure with flowing Ar carrier gas was 1 Torr. This pressure was measured by a capacitance manometer (Baratron 121A, MKS).

Each reagent was dosed into the constant stream of Ar carrier gas. The chlorination precursor was sulfuryl chloride (SO_2Cl_2 , 97%, Sigma-Aldrich). The pressure transients during the SO_2Cl_2 exposures were 100 mTorr, as defined by a metering valve (SS-4BMG, Swagelok). The ligand-addition precursor was triethylphosphine (PEt₃, 99%, Sigma-Aldrich). Pressure transients were ~10 mTorr for PEt₃ exposures without a metering valve. Thermal ALE experiments were performed with an exposure of 1 s for both precursors (SO_2Cl_2 and PEt₃). The Ar purge was 1000 s following each SO_2Cl_2 and PEt₃ exposure.

The quartz crystals used for the QCM studies (polished, RC cut, 6 MHz, Phillip Technologies) were coated with ~5000 Å of gold

deposited by electron beam deposition on top of a \sim 200 Å chromium metal adhesion layer. The gold-coated crystal was placed in a sensor head (Inficon) and sealed with a high-temperature silver epoxy (Epo-Tek H21D, Epoxy Technology Inc.). The QCM head was placed in the isothermal region of the reactor.

A constant Ar gas flow on the back of the QCM was used to prevent interaction of precursors with the backside of the QCM crystal. The changes in resonant frequency of the quartz crystal were recorded and converted to mass using a thin-film deposition monitor (Maxtek TM-400, Inficon). The QCM has a precision of $\sim 1 \text{ ng/cm}^2$. The gold-coated crystal was maintained in the reactor at temperature to equilibrate for at least 4 h before starting experiments.

Additional QCM experiments on Cu were performed with Cu QCM samples. On top of the Au-coated RC cut QCM samples, an additional 200 Å of Cr was deposited to act as a diffusion barrier. Subsequently, 2000 Å of Cu was deposited on top of the Cr film. Both the Cr and Cu were deposited by thermal evaporation. There was no vacuum break between the Cr and Cu deposition.

II.III. Transmission Electron Microscopy (TEM) Studies. TEM images of Au nanoparticles were collected on a Tecnai ST20 200 kV TEM with a LaB $_6$ electron gun and a $2k \times 2k$ BM-Orius CCD camera. Dilute Au nanopowder samples were prepared by placing a small amount of powder in ~5 mL of isopropanol and sonicating for 30 min. This solution was dropped on a 200 mesh Cu TEM grid (CF-200-Cu, Electron Microscopy Services). ImageJ software was used to process the images. 47

II.IV. Quadrupole Mass Spectrometry (QMS) Studies. QMS studies were performed in a reactor that has been used previously to investigate volatile etch products during ALE.³⁰ This reactor includes two nested gas inlet lines that meet just before the powder bed. This geometry minimizes cross-contamination in the chamber foreline. The reactor was designed to allow etch products to expand into vacuum and form a molecular beam.⁸ The beam then passes through a skimmer and flows into a differentially pumped region with a line of sight to the QMS ionizer to maximize sensitivity.⁸ A detailed description of the reactor can be found in previous publications.^{8,30}

The nanopowders used in these QMS experiments were Au (<100 nm particle size, 99.9% trace metals basis, Sigma), Cu (70 nm, 99.9%, metal basis, US-Nano), and Ni (<150 μ m, 99.99% metals basis, Sigma). Powder masses were weighed before and after exposure to the ALE reactants to determine material loss. Typical initial powder masses loaded into the sample holder were between 32 and 79 mg. Etch rates cannot be directly determined from QMS experiments on powders due to the range of particle sizes and shapes. However, mass loss is a sign of material removal.

During these experiments, the combined ultrahigh purity N_2 gas from the two reactant channels flowed through the metal powder at a rate of 5.3 sccm. This N_2 gas flow produced a pressure of ≈ 2.7 Torr in the sample holder. The N_2 gas served as both a carrier and purge gas. The partial pressure of SO_2Cl_2 (97%, Sigma) and triethylphosphine (99%, STREM) flowing through the metal powder was ≈ 2.6 Torr. Sulfuryl chloride is toxic, corrosive, a lachrymator, and releases HCl upon contact with water. Triethylphosphine is pyrophoric. Each precursor was loaded under inert atmosphere before connection to the reactor manifold.

Experiments were conducted with 120 s exposures of each precursor gas. A purge time of 600 s was employed after each precursor exposure to allow N_2 gas to purge the powder bed. The temperature of the powder bed was 150 °C. A sequence of one PEt₃ exposure, followed by three cycles of sequential SO_2Cl_2 and PEt₃ exposures were performed on the Au, Cu, and Ni powders. Separate experiments on Au powders were performed using PXRD, TEM, and X-ray photoelectron spectroscopy (XPS) analysis after seven cycles of sequential SO_2Cl_2 and PEt₃ exposures.

Two other separate experiments for XPS analysis were performed using seven sequential SO_2Cl_2 and PEt_3 exposures followed by one final SO_2Cl_2 exposure. Another experiment was conducted, where seven consecutive exposures of SO_2Cl_2 were performed on the Au powder. In all of these experiments, the temperature and dosing sequence were identical. A sequence of one PEt_3 exposure, followed

by two cycles of sequential SO_2Cl_2 and PEt_3 exposures was performed on the Cu powders. These experiments on the Cu nanopowder clogged the sample holder after two cycles of sequential SO_2Cl_2 and PEt_3 exposures.

The isotopic distributions of the volatile etch products were calculated from the naturally occurring isotopic abundances of the compound. For example, for $\operatorname{Cu_2Cl_2}(\operatorname{PEt_3})_2$, both isotopes of $\operatorname{Cu}(^{63}\operatorname{Cu},^{65}\operatorname{Cu})$, both isotopes of $\operatorname{Cl}(^{35}\operatorname{Cl},^{37}\operatorname{Cl})$, and both isotopes of $\operatorname{C}(^{12}\operatorname{C},^{13}\operatorname{C})$ were used to generate the expected isotopic patterns in the QMS scans based on natural isotopic abundances. The expected relative abundances for all of the volatile etch products were calculated for each m/z value. QMS scans were conducted with an m/z range from 2 to 500 with 1 s per scan.

II.V. XPS Studies. XPS was performed on Au nanopowder samples using a PHI 5600 instrument. A monochromatic Al $K\alpha$ source (1486.6 eV) was used to collect survey scans with a pass energy of 93.9 eV and a step size of 0.4 eV/step. Higher resolution scans were performed on the Au 4f region using a pass energy of 2.95 eV and a step size of 0.025 eV/step. The dwell times for both the survey scans and the high-resolution scans were 50 ms/step. All spectra were referenced to the adventitious carbon peak centered at 285 eV. The XPS data were collected using Auger Scan (RBD Instruments) software and analyzed using CasaXPS.

II.VI. Theoretical Methods. Single point energies, geometry optimizations, and frequency calculations were performed with Gaussian 16.⁴⁸ Each relevant species was optimized with UB3LYP/sdd before high-accuracy energies were calculated at the UCCSD/sdd level of theory.^{49–53} Following established methods of statistical mechanics, these values were used to calculate the change in Gibbs free energy for the proposed reactions.⁹ To best represent experiments, these calculations were performed at 150 °C.

This methodology makes a molecular approximation that is reasonable for molecular solids such as metal chlorides and ligated products. However, the metal powders used in the first experimental step are poorly represented with this approximation. Consequently, the application of SO_2Cl_2 to pure metals was omitted from theoretical study in this work.

III. RESULTS AND DISCUSSION

III.I. QCM Experiments. QCM studies were performed on Au-coated quartz crystal samples at 125 and 150 °C to confirm material loss resulting from alternating SO_2Cl_2 and PEt_3 exposures. Figure 2 shows an X-ray diffraction pattern for the Au film on the QCM sensor. Peaks for cubic Au (COD card number 00-901-3035) and α -quartz (COD card number 00-101-1176) matched the peaks in Figure 2. The peak at 2θ =

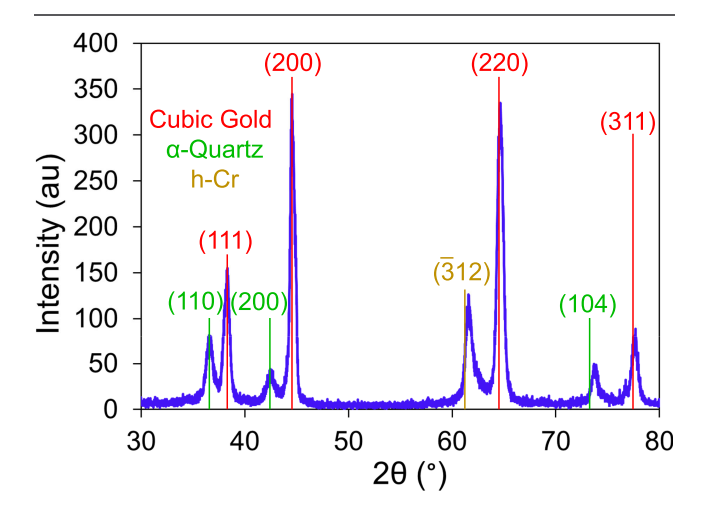


Figure 2. XRD scan of initial gold film on α -quartz QCM substrate. Diffraction peaks are consistent with cubic crystalline gold.

 61.5° is likely attributed to the Cr metal adhesion layer between the Au coating and the quartz crystal. Possible candidates are Cr($\overline{3}12$) (COD card number 00-901-4261) or possibly CrO₃(331) (COD card number 00-153-9922).

Figure 3a shows QCM results for 30 cycles of Au ALE using alternating SO₂Cl₂ and PEt₃ exposures at 125 °C. The pulse

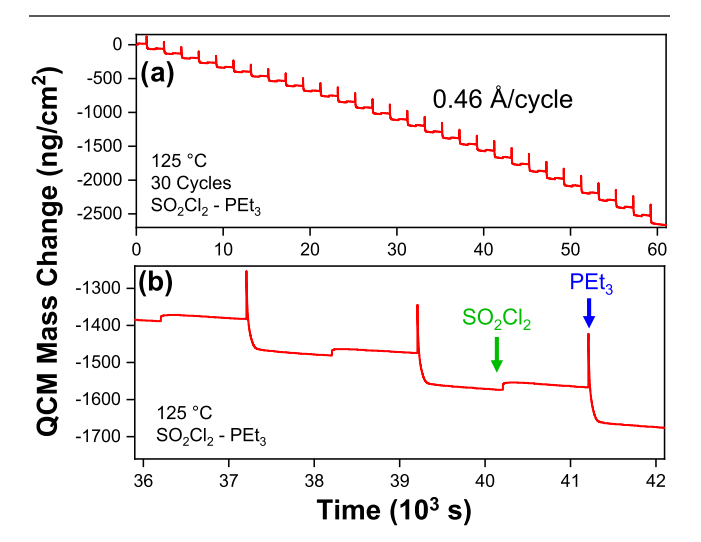


Figure 3. (a) QCM mass change versus time during sequential SO_2Cl_2 and PEt_3 exposures during Au ALE at 125 °C. Etch rate is 0.46 Å/cycle using the cubic gold density of 19.32 g/cm³. (b) Expanded view of QCM mass change over three cycles of Au ALE in panel (a).

sequence was (1, 1000, 1, 1000), where the SO_2Cl_2 and PEt_3 exposures are both 1 s and the Ar purge times following each reactant exposure are both 1000 s. The Au etching begins immediately with the first Au ALE cycle with no etch delay. The mass decreases linearly with time during the sequential SO_2Cl_2 and PEt_3 exposures. The etch rate is 88.5 ng/cm²/cycle. This etch rate is equivalent to 0.46 Å/cycle based on the Au density of 19.32 g/cm³.

Figure 3b shows an expanded view of three Au ALE cycles from the QCM results in Figure 3a. There is a mass increase during each SO_2Cl_2 exposure. This mass increase is consistent with SO_2Cl_2 adding Cl to the Au surface to form AuCl, as shown in Figure 1. In contrast, there is a mass decrease during each PEt_3 exposure. This mass decrease is consistent with the removal of the gold by ligand addition, as shown in Figure 1. The proposed reactions during Au ALE are

$$(A)2Au + SO2Cl2(g) \rightarrow 2AuCl + SO2(g)$$
 (1)

$$(B)AuCl + PEt_3(g) \rightarrow AuClPEt_3(g)$$
 (2)

During each SO_2Cl_2 exposure, the initial mass increase is followed by a slow mass decrease during each purge step. This behavior indicates that the chlorinated gold is unstable, possibly reducing after the initial gold chloride formation. At the beginning of each PEt_3 exposure, a mass gain can be observed that is followed quickly by a large mass loss. This behavior is consistent with the initial adsorption of PEt_3 onto the chlorinated Au surface. The initial adsorption is followed by the rapid release of volatile gold etch products. In addition, a gradual mass loss occurs after the PEt_3 exposures. This gradual mass loss is consistent with the slow desorption of the etch products after the PEt_3 exposure.

QCM results for 30 cycles of Au ALE using alternating SO_2Cl_2 and PEt_3 exposures at 150 °C are displayed in Figure 4a. Similar to the results at 125 °C in Figure 3a, the Au etching

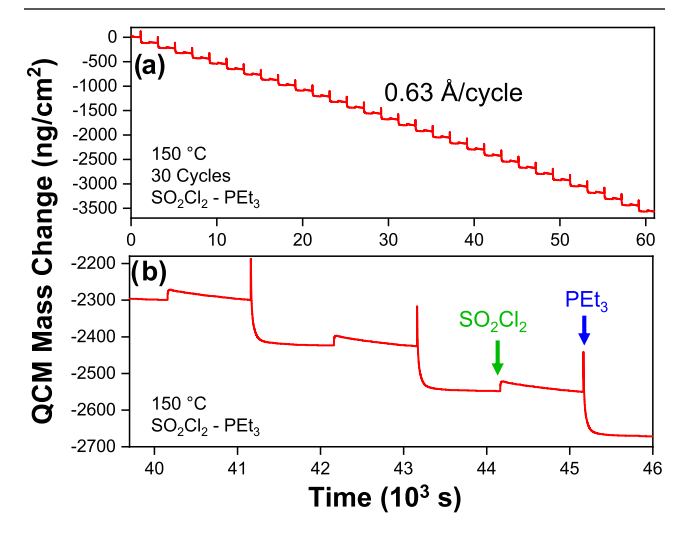


Figure 4. (a) QCM mass change versus time during sequential SO_2Cl_2 and PEt_3 exposures during Au ALE at 150 °C. Etch rate is 0.63 Å/cycle. (b) Expanded view of QCM mass change over three cycles of Au ALE in panel (a).

begins immediately, with no etch delay. The mass decreases linearly with time during the sequential SO_2Cl_2 and PEt_3 exposures with an etch rate of 121.3 ng/cm²/cycle. This etch rate is equivalent to 0.63 Å/cycle based on the Au density of 19.32 g/cm³.

Figure 4b shows an expanded view of three Au ALE cycles from the QCM results at 150 $^{\circ}$ C in Figure 4a. Similar to the results in Figure 3b, there is a mass increase during each SO_2Cl_2 exposure and a mass decrease during each PEt_3 exposure. At the higher etch temperature of 150 $^{\circ}$ C, the gradual mass changes after the SO_2Cl_2 and PEt_3 exposures are smaller. The etch products desorb more quickly after the reactant exposures at this higher temperature.

At least five separate experiments were performed for Au ALE at each temperature over seven QCM units. The average etch rates were 1.54 ± 0.38 , 0.36 ± 0.30 , 0.71 ± 0.56 , 0.44 ± 0.16 , and 0.88 ± 0.76 Å/cycle at 75, 100, 125, 150, and 175 °C, respectively. The error bars reflect the standard deviation in the etch rates determined for each experiment. These variations can be partially attributed to the experimental order and different QCM units. The large average etch rate at 75 °C is not understood at this time. The most consistent QCM results were observed at 150 °C. Consequently, 150 °C was chosen as the temperature for QMS studies and calculations.

III.II. TEM and PXRD Experiments. To confirm the proposed reaction mechanism shown in Figure 1, QMS studies were performed during sequential exposures of SO₂Cl₂ and PEt₃ on Au nanopowder at 150 °C. This Au nanopowder was characterized before and after ALE experiments in the QMS reactor. Figure 5a shows a TEM image of an initial Au nanoparticle. Figure 5b displays a TEM image of an Au nanoparticle after exposure to 7 AB cycles of SO₂Cl₂ and PEt₃ at 150 °C. The Au nanoparticles were highly agglomerated, and particles on the edge of these agglomerates were used for TEM analysis.

Analysis of low magnification TEM images revealed an average agglomerate diameter of 334 nm. Crystalline

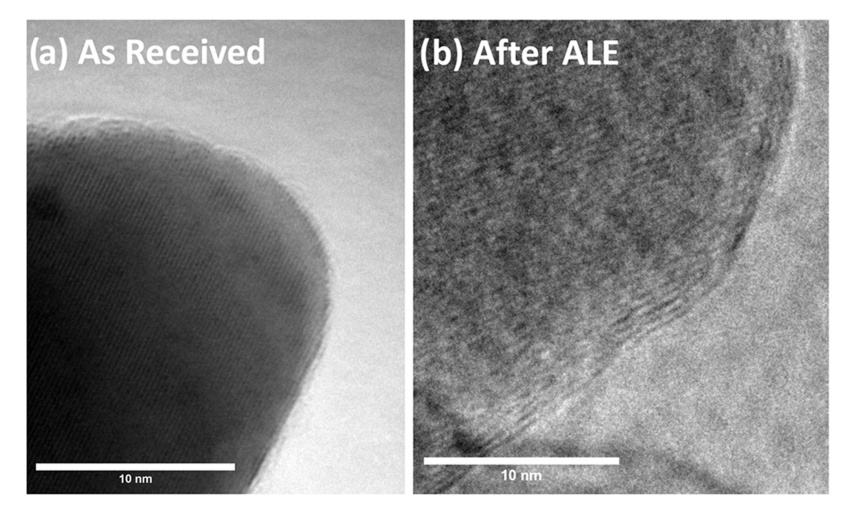


Figure 5. TEM images of Au nanoparticles: (a) as received and (b) after 7 Au ALE cycles at 150 °C. Au nanoparticles are crystalline, with a smooth surface that is not roughened after Au ALE chemistry.

diffraction fringes were observed for Au nanoparticles shown in Figure 5a before ALE and in Figure 5b after ALE. These diffraction fringes are consistent with a crystalline Au sample. All of the edges of the nanoparticles were rounded before and after ALE. This observation indicates that the effect of crystallinity on the resulting shape of the Au nanoparticles after ALE is minimal.

PXRD was also employed to verify the crystallinity of the Au nanopowder before and after ALE. PXRD patterns are shown in Figure 6a,b for the Au nanopowder before and after 7 AB

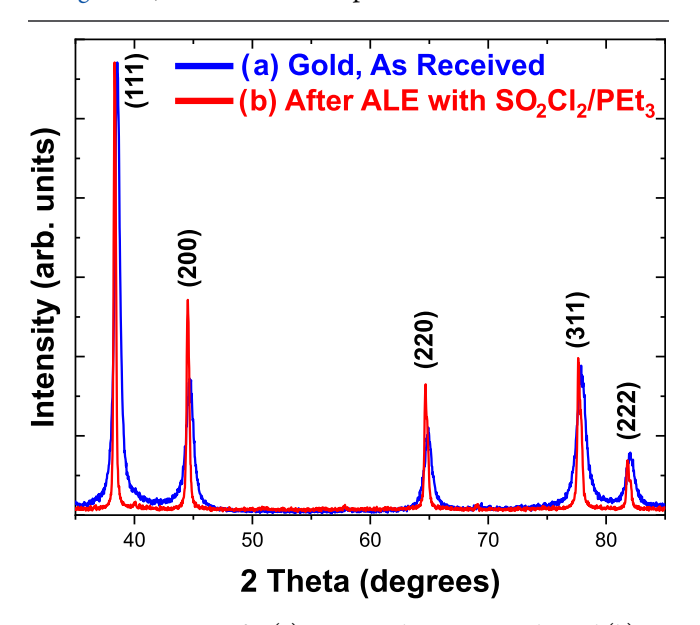


Figure 6. PXRD scans for (a) as-received Au nanopowder and (b) Au nanopowder after 7 Au ALE cycles at 150 °C. Intensities were normalized to the (111) peak.

cycles of Au ALE chemistry using SO_2Cl_2 and PEt_3 at $150\,^{\circ}C$, respectively. Both samples display peaks consistent with highly crystalline cubic Au. The PXRD pattern matches the diffraction pattern of the Au film used for QCM experiments shown in Figure 2.

The as-received Au nanopowder had an average particle size of 21.66 nm based on the diffraction peak width using the Scherrer equation. After the 7 ALE cycles, the diffraction peak

width was narrower and the average particle size increased to 65.49 nm. The Au ALE may be producing a sintering effect by redistributing Au from the small nanoparticles to the larger nanoparticles. Au redistribution could occur by the reverse of the reaction in eq 2. The resulting AuCl surface species would then need to undergo disproportionation and AuCl₃ desorption, as discussed in Section III.IV.

III.ÎII. QMS Investigations. QMS experiments were performed to determine the volatile products during Au ALE. Figure 7 shows the mass spectrum during a PEt₃

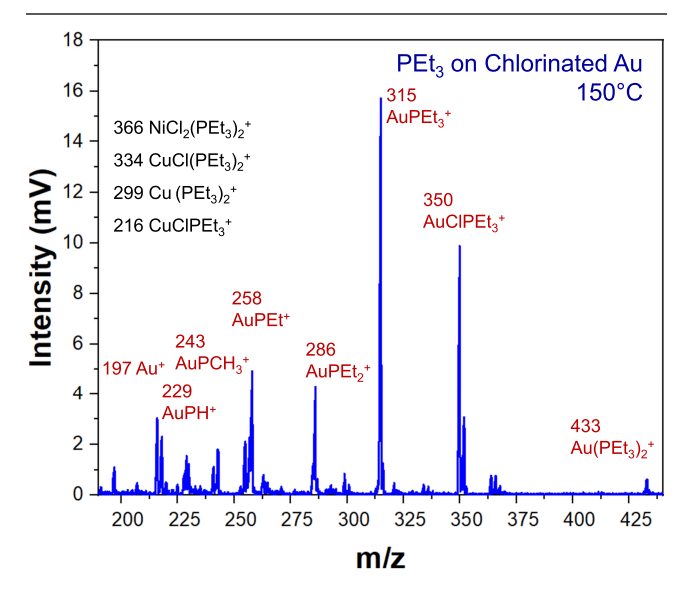


Figure 7. QMS results showing ion signal intensities after ligand addition between PEt_3 and SO_2Cl_2 -chlorinated Au nanopowders at 150 °C.

exposure on Au nanopowder after SO_2Cl_2 chlorination at 150 °C. The major volatile etch species is $AuClPEt_3$, which ionizes to produce the $AuClPEt_3^+$ ion species at m/z 350. The main ion intensity from the electron impact ionization of $AuClPEt_3$ is the $AuPEt_3^+$ ion species at m/z 315.

Figure 7 also reveals additional cracking fragments from the electron impact ionization of AuClPEt₃. AuPEt₂⁺ and AuPEt⁺ are observed at m/z 286 and 258, respectively. Au⁺ is also detected at m/z 197. Another minor peak assigned to

Au(PEt₃)₂⁺ is observed at m/z 433. However, AuCl(PEt₃)₂⁺ at m/z 468 was not observed as a possible parent of Au(PEt₃)₂⁺. No Au-containing etch products were observed during PEt₃ exposures prior to SO₂Cl₂ chlorination of the Au nanopowder. These results indicate that chlorination is necessary to produce volatile Au-containing species.

Figure 8 shows an expansion of the mass spectrum for m/z 348–355 containing the AuClPEt₃⁺ ion intensity during PEt₃

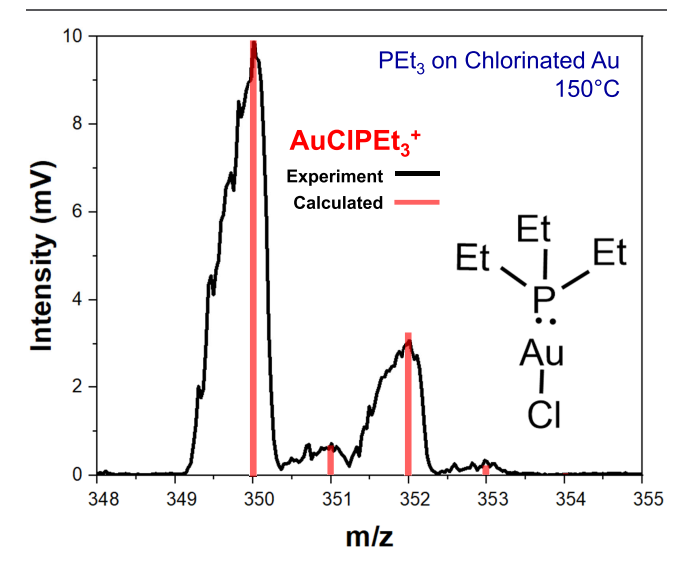


Figure 8. Ion intensities for AuClPEt₃⁺ during PEt₃ exposure to SO₂Cl₂-chlorinated Au nanopowders at 150 °C.

exposure on chlorinated Au nanopowder from Figure 7. Because Au and P have only one isotope, the isotopic signature of $AuClPEt_3^+$ is determined predominately by the ^{35}Cl and ^{37}Cl isotopes. There are only minor contributions from the ^{12}C and ^{13}C isotopes in PEt_3 . Figure 8 shows excellent agreement between the experimental QMS results and calculated intensities based on the natural isotopic abundances. The largest peak at m/z 350 is assigned to $Au^{35}ClPEt_3^+$. The second largest peak at m/z 352 is assigned to $Au^{37}ClPEt_3^+$.

The identification of the AuClPEt₃ etch product is consistent with previously observed Au compounds. AuClPEt₃ has been used as an Au ALD precursor with a reported thermal stability up to 180 °C. ⁴¹ AuClPEt₃ is consistent with the reaction given in eq 2 and shown in the Au ALE mechanism in Figure 1. This reaction is thermochemically favorable, with a free energy change of $\Delta G = -53.8$ kcal/mol at 150 °C.

Time-resolved QMS ion signal intensities can also provide useful information on the mechanism of Au ALE. Figure 9 shows the time-resolved ion intensities for PEt_3^+ , $AuPEt_3^+$, $SO_2Cl_2^+$, and SO_2^+ during three alternating PEt_3 and SO_2Cl_2 exposures on fresh Au nanopowder at 150 °C. $AuPEt_3^+$ is the largest ion intensity from the electron impact dissociation of $AuClPEt_3$ and is a proxy for the $AuClPEt_3$ etch product. One PEt_3 dose was performed prior to the alternating exposures of SO_2Cl_2 and PEt_3 . At t=3 min, Figure 9 reveals that no $AuPEt_3^+$ ion intensity is observed during PEt_3 exposure prior to chlorination. This behavior confirms that chlorination is necessary to volatilize Au-containing species.

Some $\mathrm{AuPEt_3}^+$ ion intensity is briefly observed at t=14 min at the beginning of the first $\mathrm{SO_2Cl_2}$ dose. This $\mathrm{AuPEt_3}^+$ ion intensity provides evidence that $\mathrm{PEt_3}$ was adsorbed on the surface of the Au powder. Chlorination by $\mathrm{SO_2Cl_2}$ then

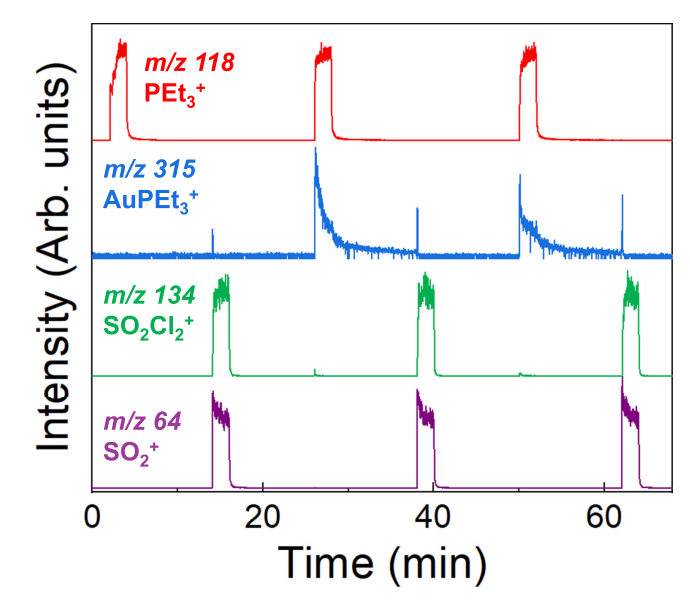


Figure 9. Time-dependent ion intensities for PEt_3^+ , $AuPEt_3^+$, $SO_2Cl_2^+$, and SO_2^+ during three alternating PEt_3 and SO_2Cl_2 exposures on fresh Au nanoparticles at 150 °C.

enabled volatilization of some AuClPEt₃. However, the appearance of the AuPEt₃⁺ ion intensity was reduced rapidly within 3 s of the SO_2Cl_2 exposure. The time-resolved signal intensities of SO_2^+ and $SO_2Cl_2^+$ are also complementary. The SO_2^+ ion intensity at m/z 64 peaks at early times and the $SO_2Cl_2^+$ ion intensity at m/z 134 is the largest at the end of the SO_2Cl_2 dose. This behavior is evidence of SO_2Cl_2 reacting with Au to form AuCl and releasing SO_2 .

A large signal for the AuClPEt₃ etch product, as indicated by the AuPEt₃⁺ ion intensity at m/z 315, is observed during the first PEt₃ dose after chlorination. This signal increases at the beginning of the PEt₃ dose and decreases slowly over the course of the PEt₃ dose. The AuPEt₃⁺ ion intensity also slowly decreases after the PEt₃ dose. The AuPEt₃⁺ ion intensity does not reach background levels during the 600 s purge after each PEt₃ dose. This behavior suggests that the desorption of AuClPEt₃ is slow.

The sample is again exposed to another SO_2Cl_2 dose at t=38 min. The $AuPEt_3^+$ ion signal rises and falls quickly, similar to the behavior on the first SO_2Cl_2 dose. This behavior suggests that residual PEt_3 on the surface of the Au powder is removed by SO_2Cl_2 . This spike in intensity at the beginning of each SO_2Cl_2 dose also coincides with a spike of PEt_3Cl^+ ion intensity at m/z 153. This observation may be evidence of direct chlorination of residual PEt_3 on the Au surface. The rapid removal of PEt_3 surface species is consistent with the spike observed for the $AuPEt_3^+$ ion signal.

The sample is then exposed to the third PEt₃ dose at t = 50 min. The response to this PEt₃ dose is similar to the second PEt₃ dose at t = 26 min. The PEt₃ dose again yields AuClPEt₃ etch product, as monitored by the AuPEt₃⁺ ion signal. Finally, the third SO₂Cl₂ dose at t = 62 min generates a response similar to the second SO₂Cl₂ dose at t = 38 min.

III.IV. XPS Experiments. XPS was used to investigate the Au surface of the Au nanopowders after different stages during Au ALE. Figure 10 shows the XPS spectra in the Au 4f region of four Au nanopowder samples. Figure 10a shows the asreceived Au nanopowders. Figure 10b displays the Au nanopowders after exposure to 7 Au ALE cycles using

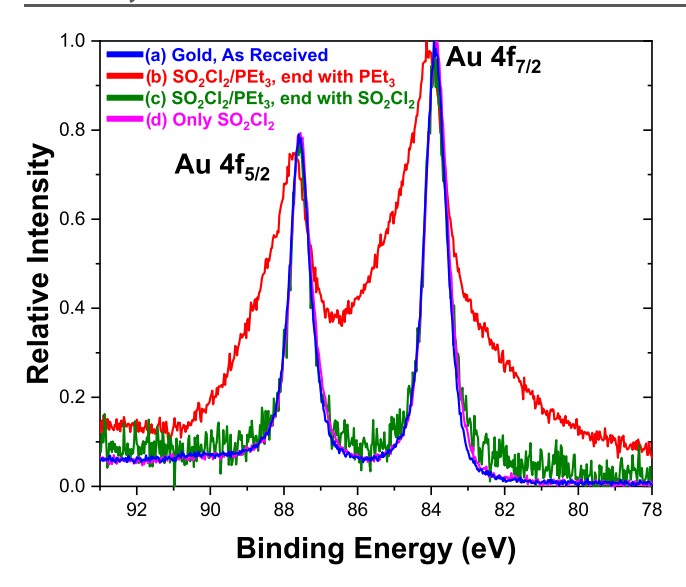


Figure 10. XPS spectra of the Au 4f region: (a) as-received Au nanopowder; (b) after Au nanopowder was exposed to 7 ALE cycles using sequential SO_2Cl_2 and PEt_3 exposures at 150 °C; (c) after Au nanopowder was exposed to 7 ALE cycles using sequential SO_2Cl_2 and PEt_3 exposures at 150 °C and ending with one additional SO_2Cl_2 exposure; and (d) after Au nanopowder was exposed to 7 SO_2Cl_2 exposures at 150 °C.

sequential SO_2Cl_2 and PEt_3 exposures at 150 °C. Figure 10c shows the Au nanopowders after exposure to 7 Au ALE cycles at 150 °C and ending with one additional SO_2Cl_2 exposure. Figure 10d displays the Au nanopowders after exposure to 7 consecutive SO_2Cl_2 exposures at 150 °C.

The Au $4f_{7/2}$ peak for metallic Au⁰ has a binding energy of 83.9 eV.^{54,55} The major Au $4f_{7/2}$ peak for all four samples in Figure 10 have binding energies between 83.85 and 84.13 eV. These binding energies are consistent with predominantly Au⁰ for all of the samples. The Au nanopowder sample exposed to the Au ALE chemistry and ending with a PEt₃ exposure has a shoulder at higher binding energies >84 eV. The shoulder extends to binding energies up to 86 eV. This binding energy shift is consistent with Au¹⁺ because Au¹⁺ has a higher binding energy than Au⁰ by +2.3 eV.⁵⁶ The most likely candidate species for this Au¹⁺ shoulder is AuClPEt₃. The reported Au $4f_{7/2}$ binding energy for AuClPEt₃ is 85.2 eV.⁵⁷

The higher binding energy shoulder is not observed for the other three samples in Figure 10. Observing Au⁰ on samples exposed to Au ALE chemistry and ending with SO₂Cl₂ and on samples exposed only to SO₂Cl₂ indicates that Au chlorides formed on the Au surface may not be thermally stable. AuCl₃ may quickly decompose to AuCl + Cl₂. AuCl surface species may undergo a disproportionation according to ^{58,59}

$$3AuCl \rightarrow AuCl_3 + 2Au$$
 (3)

The AuCl $_3$ may then desorb as Au $_2$ Cl $_6$ at 150 $^{\circ}$ C. 60

III.V. Experiments on Cu and Ni Etching. Cu and Nicontaining etch products were also detected while conducting the QMS experiments on Au ALE. For example, additional minor species are present in Figure 7 during the QMS experiments for PEt₃ doses on chlorinated Au powder. The peaks at m/z 334, 299, and 216 were assigned to CuCl- $(PEt_3)_2^+$, Cu $(PEt_3)_2^+$, and CuClPEt₃⁺, respectively. The peaks centered at m/z 366 were assigned to NiCl₂ $(PEt_3)_2$. These Cu and Ni species were attributed to the etching of copper

ConFlat gaskets and nickel-containing stainless steel in the reactor by the sequential SO_2Cl_2 and PEt_3 exposures. The detection of these peaks motivated separate experiments on Cu and Ni etching at 150 °C to establish the generality of the chlorination and ligand-addition mechanism for metal thermal ALE

A QMS experiment on Cu metal powder was conducted under the same conditions as for Au ALE. After chlorination, the mass spectrum showed $\mathrm{Cu}_2\mathrm{Cl}_2(\mathrm{PEt}_3)_2^+$ dimer species centered at m/z 434. Smaller fragments resulting from electron impact ionization of the $\mathrm{Cu}_2\mathrm{Cl}_2(\mathrm{PEt}_3)_2$ dimer species were also monitored for $\mathrm{Cu}_2\mathrm{Cl}(\mathrm{PEt}_3)_2^+$ at m/z 397 and for $\mathrm{CuCl}(\mathrm{PEt}_3)_2^+$ at m/z 334. Fragmentation of the $\mathrm{Cu}_2\mathrm{Cl}_2(\mathrm{PEt}_3)_2$ dimer or the $\mathrm{CuClPEt}_3$ monomer also led to the observation of $\mathrm{Cu}(\mathrm{PEt}_3)_2^+$ at m/z 299, $\mathrm{CuClPEt}_3^+$ at m/z 216, and $\mathrm{Cu}(\mathrm{PEt}_3)_2^+$ at m/z 181.

Figure 11 shows an expanded view of the ion intensities for $\text{Cu}_2\text{Cl}_2(\text{PEt}_3)_2^+$. The experimental measurement is in good

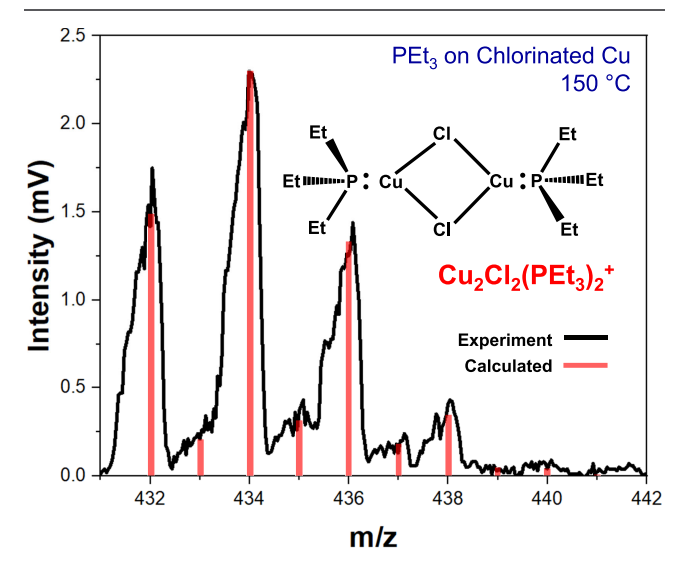


Figure 11. Ion intensities for Cu₂Cl₂(PEt₃)₂⁺ during PEt₃ exposure to SO₂Cl₂-chlorinated Cu nanopowder at 150 °C.

agreement with the calculated signal based on the natural abundance of the isotopes. The largest intensity peak is attributed to a combination of $^{63}\text{Cu}_2^{35}\text{Cl}_3^{7}\text{Cl}(\text{PEt}_3)_2$ and $^{63}\text{Cu}_3^{65}\text{Cl}_2^{35}\text{Cl}_2(\text{PEt}_3)_2$ at m/z 434. The second largest peak is attributed to $^{63}\text{Cu}_2^{35}\text{Cl}_2(\text{PEt}_3)_2$ at m/z 432. Other peaks are defined by the isotopes of Cu, Cl, and ^{12}C and ^{13}C in the Et groups of PEt₃.

The observation of the $Cu_2Cl_2(PEt_3)_2$ dimer is consistent with the reaction:

$$2CuCl + 2PEt_3 \rightarrow Cu_2Cl_2(PEt_3)_2 \tag{4}$$

This reaction is thermochemically favorable with a free energy change of $\Delta G = -147.0$ kcal/mol at 150 °C. This free energy change is equivalent to $\Delta G = -73.5$ kcal/mol per Cu atom. The free energy change for the corresponding monomer product, CuClPEt₃, was also calculated based on the reaction

$$CuCl + PEt_3 \rightarrow CuClPEt_3 \tag{5}$$

This reaction is thermochemically favorable with a free energy change of $\Delta G = -41.8$ kcal/mol at 150 °C. Based on the larger free energy change per Cu atom for the dimer species, the etch

product should favor the dimer species in agreement with the experimental observations.

The structure of the $Cu_2Cl_2(PEt_3)_2$ dimer species likely involves bridging chlorines between the Cu atoms. Crystallographic studies of $Cu_2Cl_2(PPh_3)_2(4,4'$ -bipyridine) reported a structure where two chlorine atoms bridge the two Cu atoms. Additionally, electron diffraction studies of volatile Cu_3Cl_3 clusters also report a structure where each Cl bridges between two Cu atoms.

Additional QCM experiments also demonstrated that sequential SO_2Cl_2 and PEt_3 exposures can etch Cu thin films. For these Cu ALE experiments, the QCM sample was coated with 2000 Å of Cu metal deposited by thermal evaporation. The Cu was deposited on top of a 200 Å Cr diffusion barrier layer on the underlying Au-coated RC cut QCM sample. GI-XRD was performed on the Cu QCM samples. XRD peaks were observed at $2\theta = 43.3$, 50.5, and 74.2° , consistent with the (111), (200), and (220) planes, respectively, of cubic copper (COD card number 00-410-5681). Other experiments of Cu etching with Cu deposited directly on Au with no Cr diffusion barrier were inconsistent because of alloying between Au and Cu.

Figure 12 shows the QCM results for a Cu film exposed to 30 cycles of alternating SO₂Cl₂ and PEt₃ exposures at 100 °C.

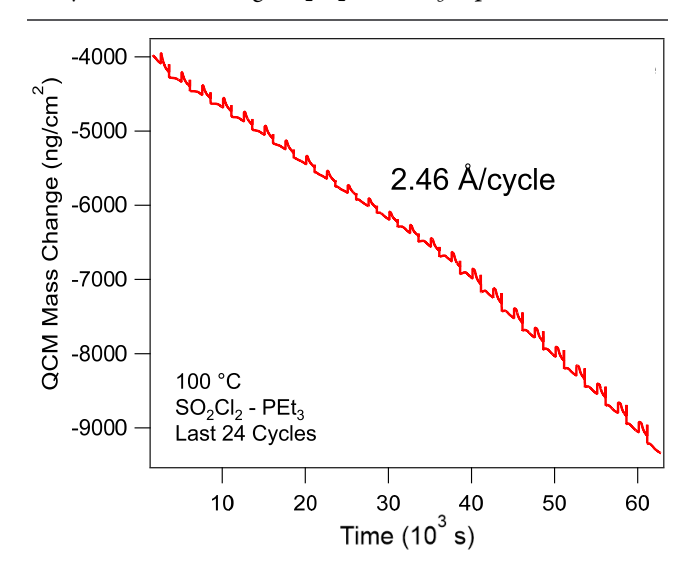


Figure 12. (a) QCM mass change versus time during sequential SO_2Cl_2 and PEt_3 exposures during Cu ALE at 100 °C. Etch rate is 2.46 Å/cycle using a copper density of 8.96 g/cm³.

This experiment for Cu ALE used the same dosing and purge sequence as the previous experiments for Au ALE. The QCM results are consistent with a mass loss of 220.2 ng/(cm² cycle) or an etch rate of 2.46 Å/cycle. Cu ALE was observed at temperatures between 75 and 175 °C. The most consistent etching temperature for the Cu ALE experiments was 100 °C. During the QMS experiments, trace cracks of the Cu etch product at m/z 216 attributed to CuCl(PEt₃)⁺ were observed at temperatures as low as 100 °C, in agreement with the QCM experiments.

QMS experiments were also performed on Ni nanopowder to determine the identity of the Ni etch product. Figure 13 shows the mass spectrum of $NiCl_2(PEt_3)_2^+$ ion signal during a PEt₃ exposure on SO_2Cl_2 -chlorinated Ni at 150 °C. The asreceived Ni nanopowder sample was confirmed through PXRD to be cubic Ni (COD card number 00-151-2526). Compared

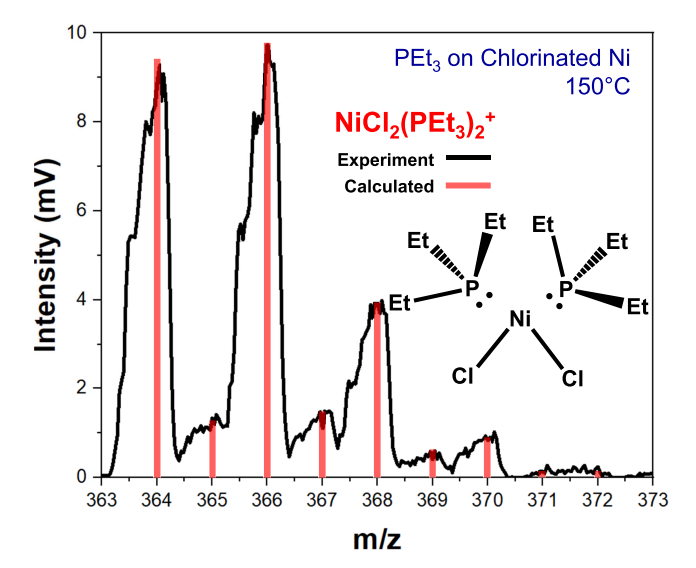


Figure 13. Ion intensity for NiCl₂(PEt₃)₂⁺ during PEt₃ exposure to SO₂Cl₂-chlorinated Ni nanopowder at 150 °C.

with the earlier results in Figure 7, the signal intensity at m/z 366 in Figure 13 increased 10-fold under identical reaction conditions. The peak at m/z 366 increased in intensity from \sim 1 mV in Figure 7 to \sim 10 mV in Figure 13.

The largest ion intensity at m/z 366 is attributed to a combination of $^{60}\mathrm{Ni}^{35}\mathrm{Cl}_2(\mathrm{PEt}_3)_2$ and $^{58}\mathrm{Ni}^{35}\mathrm{Cl}^{37}\mathrm{Cl}(\mathrm{PEt}_3)_2$. The second largest ion intensity is consistent with $^{58}\mathrm{Ni}^{35}\mathrm{Cl}_2(\mathrm{PEt}_3)_2$ at m/z 364. The third largest ion intensity at m/z 368 is attributed to a combination of $^{60}\mathrm{Ni}^{35}\mathrm{Cl}^{37}\mathrm{Cl}(\mathrm{PEt}_3)_2$, $^{58}\mathrm{Ni}^{37}\mathrm{Cl}_2(\mathrm{PEt}_3)_2$, and $^{62}\mathrm{Ni}^{35}\mathrm{Cl}_2(\mathrm{PEt}_3)_2$. Other cracks are explained by different numbers of $^{12}\mathrm{C}$ and $^{13}\mathrm{C}$ in the ethyl groups of $^{12}\mathrm{C}$ 3.

The observation of $NiCl_2(PEt_3)_2$ is consistent with the reaction

$$NiCl_2 + 2PEt_3 \rightarrow NiCl_2(PEt_3)_2$$
 (6)

This reaction is thermochemically favorable with a free energy change of $\Delta G = -88.6 \text{ kcal/mol}$ at 150 °C. The large free energy change is consistent with the experimental observation of trace NiCl₂(PEt₃)₂ above noise levels during all experiments resulting from chlorinated Ni in the Type 304 stainless steel chamber. The proposed structure of NiCl₂(PEt₃)₂ shown in Figure 13 is similar to the previously reported NiCl₂(PMe₃)₂ volatile species from the reaction of NiCl₂ with PMe₃. NiCl₂(PEt₃)₂ is also reported as a Ni ALD precursor with a melting point of \sim 90 °C. 63

IV. CONCLUSIONS

Gold thermal ALE was demonstrated using sequential chlorination and ligand-addition reactions at temperatures from 75 to 175 °C. SO_2Cl_2 was employed during the chlorination reaction to modify the gold surface. PEt $_3$ was used during the volatile release reaction to yield gold etch products. The most reliable etch rate measured by QCM experiments was 0.44 \pm 0.16 Å/cycle at 150 °C. QMS studies identified the volatile Au-containing etch product as AuClPEt $_3$ at 150 °C.

The QCM studies revealed the mechanism for Au ALE during the sequential SO_2Cl_2 and PEt_3 exposures. The mass increased with each SO_2Cl_2 exposure as expected during chlorination, consistent with the formation of AuCl. Each PEt_3

exposure yielded a mass reduction. This mass reduction was consistent with the volatilization of Au-containing species resulting from ligand addition to the AuCl surface species.

QMS also monitored the time dependence of the chlorination and the ligand-addition reaction. The SO_2^+ ion intensity peaked before the $SO_2Cl_2^+$ ion intensity, consistent with SO_2Cl_2 chlorinating Au to produce SO_2 . The AuClPEt3 etch product intensity also peaked at the beginning of PEt3 doses after SO_2Cl_2 exposures. The slow decay of the AuPEt3+ ion intensity was consistent with slow desorption of the Aucontaining etch product. XPS of the powder samples after ALE showed evidence that AuClPEt3 exists on the surface of the Aupowder when Au ALE ends with the PEt3 exposure. In contrast, ending the ALE dosing sequence with SO_2Cl_2 forms a gold chloride that may decompose to form metallic gold on the surface via AuCl disproportionation.

Au nanopowder was also analyzed with TEM before and after exposure to the Au ALE chemistry. The TEM images revealed crystalline Au nanoparticles with no evidence of crystalline faceting at the edges of the particles after Au ALE. PXRD confirmed that the powder samples were cubic crystalline gold. The diffraction peaks narrowed after Au ALE, consistent with an increase in average particle size. A sintering effect may occur resulting from redeposition of AuCl from AuClPEt₃ followed by AuCl disproportionation.

QMS also identified $\text{Cu}_2\text{Cl}_2(\text{PEt}_3)_2$ and $\text{NiCl}_2(\text{PEt}_3)_2$ etch products from Cu and Ni nanopowders, respectively, concurrent with PEt3 exposures during alternating SO_2Cl_2 and PEt3 exposures. QCM studies also monitored Cu ALE using sequential SO_2Cl_2 and PEt3 exposures and measured an etch rate of 2.46 Å/cycle at 100 °C. Thermodynamic calculations demonstrated the favorability of PEt3 ligand addition to metal chlorides of Au, Cu, and Ni. The calculations were also consistent with the preferred formation of the dimer, $\text{Cu}_2\text{Cl}_2(\text{PEt}_3)_2$, instead of the monomer, Cu_2PEt_3 .

This study demonstrated that sequential chlorination and ligand-addition reactions using SO₂Cl₂ and PEt₃ can provide a useful pathway for the thermal ALE of Au, Cu, and Ni metals. This chemistry could be paired with Au ALD to deposit and tune the thickness of Au films and tailor Au nanostructures for plasmonic and photonic applications. This chemistry could also provide a useful pathway for the thermal ALE of other metals with nonvolatile chlorides.

AUTHOR INFORMATION

Corresponding Author

Steven M. George — Department of Chemistry, University of Colorado, Boulder, Colorado 80309, United States; orcid.org/0000-0003-0253-9184;

Email: Steven.George@colorado.edu

Authors

Jonathan L. Partridge — Department of Chemistry, University of Colorado, Boulder, Colorado 80309, United States;
orcid.org/0000-0002-0071-9854

Jessica A. Murdzek – Department of Chemistry, University of Colorado, Boulder, Colorado 80309, United States

Virginia L. Johnson – Department of Chemistry, University of Colorado, Boulder, Colorado 80309, United States

Andrew S. Cavanagh – Department of Chemistry, University of Colorado, Boulder, Colorado 80309, United States;
orcid.org/0000-0002-6201-530X

Sandeep Sharma — Department of Chemistry, University of Colorado, Boulder, Colorado 80309, United States;
orcid.org/0000-0002-6598-8887

Complete contact information is available at: https://pubs.acs.org/10.1021/acs.chemmater.4c00485

Notes

The authors declare no competing financial interest.

ACKNOWLEDGMENTS

This work was supported in part by the Joint University Microelectronics Program (JUMP) funded by the Semiconductor Research Corporation (SRC). Funding for the QMS reactor and the QMS investigations was provided by LAM Research Corporation. The authors acknowledge the COSINC FAB facility at the University of Colorado (CU) for use of the thermal evaporation chamber for deposition of the Cu QCM samples. The authors thank Aaron Bell from the CU Geology Department for use of the Bruker D8 Powder X-ray diffractometer. The authors also thank Sadegh Yazdi and the CU Facility for Electron Microscopy of Materials (FEMM) for use of the Tecnai TEM instrument. This work utilized the Blanca condo computing resource at the CU Boulder. Blanca is jointly funded by computing users and CU Boulder. VLJ was supported by an NSF Graduate Research Fellowship under Grant DGE-2040434. S.S. was supported by NSF Grant CHE-2145209.

REFERENCES

- (1) Kanarik, K. J.; Lill, T.; Hudson, E. A.; Sriraman, S.; Tan, S.; Marks, J.; Vahedi, V.; Gottscho, R. A. Overview of Atomic Layer Etching in the Semiconductor Industry. *J. Vac. Sci. Technol. A* **2015**, 33, No. 020802.
- (2) Fischer, A.; Routzahn, A.; George, S. M.; Lill, T. Thermal Atomic Layer Etching: A Review. *J. Vac. Sci. Technol. A* **2021**, 39, No. 030801.
- (3) George, S. M. Mechanisms of Thermal Atomic Layer Etching. *Acc. Chem. Res.* **2020**, *53*, 1151–1160.
- (4) George, S. M.; Lee, Y. Prospects for Thermal Atomic Layer Etching Using Sequential, Self-Limiting Fluorination and Ligand-Exchange Reactions. *ACS Nano* **2016**, *10*, 4889–4894.
- (5) Lee, Y.; George, S. M. Atomic Layer Etching of Al₂O₃ Using Sequential, Self-Limiting Thermal Reactions with Sn(acac)₂ and Hydrogen Fluoride. *ACS Nano* **2015**, *9*, 2061–2070.
- (6) Čano, A. M.; Marquardt, A. E.; Dumont, J. W.; George, S. M. Effect of HF Pressure on Thermal Al₂O₃ Atomic Layer Etch Rates and Al₂O₃ Fluorination. *J. Phys. Chem. C* **2019**, *123*, 10346–10355.
- (7) Clancey, J. W.; Cavanagh, A. S.; Smith, J. E. T.; Sharma, S.; George, S. M. Volatile Etch Species Produced During Thermal Al₂O₃ Atomic Layer Etching, *J. Phys. Chem. C* **2020**, 124, 287–299.
- (8) Lii-Rosales, A.; Cavanagh, A. S.; Fischer, A.; Lill, T.; George, S. M. Spontaneous Etching of Metal Fluorides Using Ligand-Exchange Reactions: Landscape Revealed by Mass Spectrometry. *Chem. Mater.* **2021**, 33, 7719–7730.
- (9) Lii-Rosales, A.; Johnson, V. L.; Cavanagh, A. S.; Fischer, A.; Lill, T.; Sharma, S.; George, S. M. Effectiveness of Different Ligands on Silane Precursors for Ligand Exchange to Etch Metal Fluorides. *Chem. Mater.* **2022**, *34*, 8641–8653.
- (10) Lee, Y.; Dumont, J. W.; George, S. M. Trimethylaluminum as the Metal Precursor for the Atomic Layer Etching of Al_2O_3 Using Sequential, Self-Limiting Thermal Reactions. *Chem. Mater.* **2016**, 28, 2994–3003.
- (11) Lee, Y.; George, S. M. Thermal Atomic Layer Etching of Al_2O_3 , HfO_2 , and ZrO_2 Using Sequential Hydrogen Fluoride and Dimethylaluminum Chloride Exposures. *J. Phys. Chem. C* **2019**, 123, 18455–18466.

- (12) Lee, Y.; Huffman, C.; George, S. M. Selectivity in Thermal Atomic Layer Etching Using Sequential, Self-Limiting Fluorination and Ligand-Exchange Reactions. *Chem. Mater.* **2016**, *28*, 7657–7665.
- (13) Lee, Y.; George, S. M. Thermal Atomic Layer Etching of HfO₂ Using Hf for Fluorination and TiCl₄ for Ligand-Exchange. *J. Vac. Sci. Technol. A* **2018**, *36*, No. 061504.
- (14) Johnson, N. R.; George, S. M. WO₃ and W Thermal Atomic Layer Etching Using "Conversion-Fluorination" and "Oxidation-Conversion-Fluorination" Mechanisms. *ACS Appl. Mater. Interfaces* **2017**, *9*, 34435–34447.
- (15) Cano, A. M.; Kondati Natarajan, S.; Partridge, J. L.; Elliott, S. D.; George, S. M. Spontaneous Etching of B_2O_3 by HF Gas Studied Using Infrared Spectroscopy, Mass Spectrometry, and Density Functional Theory. *J. Vac. Sci. Technol. A* **2022**, 40, No. 022601, DOI: 10.1116/6.0001542.
- (16) Lee, Y.; George, S. M. Thermal Atomic Layer Etching of Titanium Nitride Using Sequential, Self-Limiting Reactions: Oxidation to TiO_2 and Fluorination to Volatile TiF_4 . Chem. Mater. 2017, 29, 8202–8210.
- (17) Kondati Natarajan, S.; Cano, A. M.; Partridge, J. L.; George, S. M.; Elliott, S. D. Prediction and Validation of the Process Window for Atomic Layer Etching: HF Exposure on TiO₂. *J. Phys. Chem. C* **2021**, 125, 25589–25599.
- (18) Myers, T. J.; Cano, A. M.; Lancaster, D. K.; et al. Conversion Reactions in Atomic Layer Processing with Emphasis on ZnO Conversion to $\mathrm{Al_2O_3}$ by Trimethylaluminum. *J. Vac. Sci. Technol. A* **2021**, *39*, 021001.
- (19) DuMont, J. W.; Marquardt, A. E.; Cano, A. M.; George, S. M. Thermal Atomic Layer Etching of SiO_2 by a "Conversion-Etch" Mechanism Using Sequential Reactions of Trimethylaluminum and Hydrogen Fluoride. *ACS Appl. Mater. Interfaces* **2017**, *9*, 10296–10307.
- (20) Zywotko, D. R.; George, S. M. Thermal Atomic Layer Etching of ZnO by a "Conversion-Etch" Mechanism Using Sequential Exposures of Hydrogen Fluoride and Trimethylaluminum. *Chem. Mater.* **2017**, 29, 1183–1191.
- (21) Abdulagatov, A. I.; George, S. M. Thermal Atomic Layer Etching of Silicon Using O_2 , HF, and $Al(CH_3)_3$ as the Reactants. *Chem. Mater.* **2018**, 30, 8465–8475.
- (22) Abdulagatov, A. I.; George, S. M. Thermal Atomic Layer Etching of Silicon Nitride Using an Oxidation and "Conversion Etch" Mechanism. *J. Vac. Sci. Technol. A* **2020**, *38*, No. 022607.
- (23) Abdulagatov, A. I.; Sharma, V.; Murdzek, J. A.; Cavanagh, A. S.; George, S. M. Thermal Atomic Layer Etching of Germanium-Rich SiGe Using an Oxidation and "Conversion-Etch" Mechanism. *J. Vac. Sci. Technol. A* **2021**, 39, No. 022602.
- (24) Chen, J. K.-C.; Altieri, N. D.; Kim, T.; Chen, E.; Lill, T.; Shen, M.; Chang, J. P. Directional Etch of Magnetic and Noble Metals. II. Organic Chemical Vapor Etch. *J. Vac. Sci. Technol. A* **2017**, 35, No. 05C305.
- (25) Konh, M.; He, C.; Lin, X.; Guo, X.; Pallem, V.; Opila, R. L.; Teplyakov, A. V.; Wang, Z.; Yuan, B. Molecular Mechanisms of Atomic Layer Etching of Cobalt with Sequential Exposure to Molecular Chlorine and Diketones. *J. Vac. Sci. Technol. A* **2019**, 37, No. 021004.
- (26) Mohimi, E.; Chu, X. I.; Trinh, B. B.; Babar, S.; Girolami, G. S.; Abelson, J. R. Thermal Atomic Layer Etching of Copper by Sequential Steps Involving Oxidation and Exposure to Hexafluoroacetylacetone. *ECS J. Solid State Sci. Technol.* **2018**, *7*, P491–P495.
- (27) Murdzek, J. A.; Lii-Rosales, A.; George, S. M. Thermal Atomic Layer Etching of Nickel Using Sequential Chlorination and Ligand-Addition Reactions. *Chem. Mater.* **2021**, *33*, 9174–9183.
- (28) Lii-Rosales, A.; Johnson, V. L.; Sharma, S.; Fischer, A.; Lill, T.; George, S. M. Volatile Products from Ligand Addition of P(CH₃)₃ to NiCl₂, PdCl₂, and PtCl₂: Pathway for Metal Thermal Atomic Layer Etching. *J. Phys. Chem. C* **2022**, *126*, 8287–8295.
- (29) Murdzek, J. A.; Lii-Rosales, A.; George, S. M. Thermal Atomic Layer Etching of Cobalt Using Sulfuryl Chloride for Chlorination and

- Tetramethylethylenediamine or Trimethylphosphine for Ligand Addition. J. Vac. Sci. Technol. A 2023, 41, No. 032603.
- (30) Partridge, J. L.; Murdzek, J. A.; Johnson, V. L.; Cavanagh, A. S.; Fischer, A.; Lill, T.; Sharma, S.; George, S. M. Thermal Atomic Layer Etching of CoO, ZnO, Fe₂O₃, and NiO by Chlorination and Ligand Addition Using SO₂Cl₂ and Tetramethylethylenediamine. *Chem. Mater.* **2023**, 35, 2058–2068.
- (31) Chang, C.; Chang, P. Innovative Micromachined Microwave Switch with Very Low Insertion Loss. *Sens. Actuators, A* **2000**, *79*, 71–75, DOI: 10.1016/S0924-4247(99)00218-6.
- (32) Green, T. A. Gold Etching for Microfabrication. *Gold Bull.* **2014**, 47, 205–216.
- (33) Holliday, R.; Goodman, P. Going for Gold [Gold in Electronics Industry]. *IEE Rev.* **2002**, *48*, 15–19.
- (34) Ravi Sankar, A.; Lahiri, S. K.; Das, S. Performance Enhancement of a Silicon MEMS Piezoresistive Single Axis Accelerometer with Electroplated Gold on a Proof Mass. *J. Micromech. Microeng.* **2009**, *19*, No. 025008.
- (35) Amendola, V.; Pilot, R.; Frasconi, M.; Maragò, O. M.; Iati, M. A. Surface Plasmon Resonance in Gold Nanoparticles: A Review. *J. Phys.: Condens. Matter* **2017**, *29*, No. 203002.
- (36) Saha, K.; Agasti, S. S.; Kim, C.; Li, X. N.; Rotello, V. M. Gold Nanoparticles in Chemical and Biological Sensing. *Chem. Rev.* **2012**, 112, 2739–2779.
- (37) Venditti, I. Gold Nanoparticles in Photonic Crystals Applications: A Review. *Materials* **2017**, *10*, 97.
- (38) Griffiths, M. B. E.; Pallister, P. J.; Mandia, D. J.; Barry, S. T. Atomic Layer Deposition of Gold Metal. *Chem. Mater.* **2016**, *28*, 44–46.
- (39) Van Daele, M.; Griffiths, M. B. E.; Raza, A.; Minjauw, M. M.; Solano, E.; Feng, J. Y.; Ramachandran, R. K.; Clemmen, S.; Baets, R.; Barry, S. T.; et al. Plasma-Enhanced Atomic Layer Deposition of Nanostructured Gold near Room Temperature. *ACS Appl. Mater. Interfaces* **2019**, *11*, 37229–37238, DOI: 10.1021/acsami.9b10848.
- (40) Mäkelä, M.; Hatanpää, T.; Mizohata, K.; Räisänen, J.; Ritala, M.; Leskelä, M. Thermal Atomic Layer Deposition of Continuous and Highly Conducting Gold Thin Films. *Chem. Mater.* **2017**, *29*, 6130–6136.
- (41) Vihervaara, A.; Hatanpää, T.; Nieminen, H.-E.; Mizohata, K.; Chundak, M.; Ritala, M. Reductive Thermal Atomic Layer Deposition Process for Gold. *ACS Mater. Au* **2023**, *3*, 206–214.
- (42) Mäkelä, M.; Hatanpää, T.; Ritala, M.; Leskelä, M.; Mizohata, K.; Meinander, K.; Räisänen, J. Potential Gold(I) Precursors Evaluated for Atomic Layer Deposition. *J. Vac. Sci. Technol. A* **2017**, 35, No. 01B112.
- (43) Lee, H. B. R.; Bent, S. F. Microstructure-Dependent Nucleation in Atomic Layer Deposition of Pt on TiO₂. *Chem. Mater.* **2012**, *24*, 279–286.
- (44) Wind, R. W.; Fabreguette, F. H.; Sechrist, Z. A.; George, S. M. Nucleation Period, Surface Roughness, and Oscillations in Mass Gain per Cycle During W Atomic Layer Deposition On Al₂O₃. *J. Appl. Phys.* **2009**, *105*, No. 074309.
- (45) Gertsch, J. C.; Sortino, E.; Bright, V. M.; George, S. M. Deposit and Etchback Approach for Ultrathin Al₂O₃ Films with Low Pinhole Density Using Atomic Layer Deposition and Atomic Layer Etching. *J. Vac. Sci. Technol. A* **2021**, *39*, No. 062602.
- (46) Elam, J. W.; Groner, M. D.; George, S. M. Viscous Flow Reactor with Quartz Crystal Microbalance for Thin Film Growth by Atomic Layer Deposition. *Rev. Sci. Instrum.* **2002**, *73*, 2981.
- (47) Schneider, C. A.; Rasband, W. S.; Eliceiri, K. W. NIH Image to ImageJ: 25 years of image analysis. *Nat. Methods* **2012**, *9*, 671–675.
- (48) Frisch, M. J.; T. G. W.; Schlegel, H. B.; Scuseria, G. E.; Robb, M. A.; Cheeseman, J. R.; Scalmani, G.; Barone, V.; Petersson, G. A.; Nakatsuji, H.; Li, X.; Caricato, M.; Marenich, A. V.; Bloino, J.; Janesko, B. G.; Gomperts, R.; Mennucci, B.; Hratchian, H. P.; Ortiz, J. V.; Izmaylov, A. F.; Sonnenberg, J. L.; Williams-Young, D.; Ding, F.; Lipparini, F.; Egidi, F.; Goings, J.; Peng, B.; Petrone, A.; Henderson, T.; Ranasinghe, D.; Zakrzewski, V. G.; Gao, J.; Rega, N.; Zheng, G.; Liang, W.; Hada, M.; Ehara, M.; Toyota, K.; Fukuda, R.; Hasegawa, J.;

- Ishida, M.; Nakajima, T.; Honda, Y.; Kitao, O.; Nakai, H.; Vreven, T.; Throssell, K.; Montgomery, J. A., Jr.; Peralta, J. E.; Ogliaro, F.; Bearpark, M. J.; Heyd, J. J.; Brothers, E. N.; Kudin, K. N.; Staroverov, V. N.; Keith, T. A.; Kobayashi, R.; Normand, J.; Raghavachari, K.; Rendell, A. P.; Burant, J. C.; Iyengar, S. S.; Tomasi, J.; Cossi, M.; Millam, J. M.; Klene, M.; Adamo, C.; Cammi, R.; Ochterski, J. W.; Martin, R. L.; Morokuma, K.; Farkas, O.; Foresman, J. B.; Fox, D. J. Gaussian 16, Revision C.01; Gaussian, Inc.: Wallingford CT, 2016.
- (49) Dunning, T. H.; Hay, P. J. Gaussian Basis Sets for Molecular Calculations. In *Methods of Electronic Structure Theory. Modern Theoretical Chemistry*; Schaefer, H. F., Ed.; Springer: Boston, MA, 1977; Vol. 3, pp 1–27.
- (50) Lee, C. T.; Yang, W. T.; Parr, R. G. Development of the Colle-Salvetti Correlation-Energy Formula into a Functional of the Electron-Density. *Phys. Rev. B* **1988**, *37*, 785–789.
- (51) Scuseria, G. E.; Janssen, C. L.; Schaefer, H. F. An Efficient Reformulation of the Closed-Shell Coupled Cluster Single and Double Excitation (CCSD) Equations. *J. Chem. Phys.* **1988**, 89, 7382–7387.
- (52) Scuseria, G. E.; Schaefer, H. F. Is Coupled Cluster Singles and Doubles (CCSD) More Computationally Intensive Than Quadratic Configuration-Interaction (QCISD). *J. Chem. Phys.* **1989**, 90, 3700–3703.
- (53) Weigend, F.; Ahlrichs, R. Balanced Basis Sets of Split Valence, Triple Zeta Valence and Quadruple Zeta Valence Quality for H to Rn: Design and Assessment of Accuracy. *Phys. Chem. Chem. Phys.* **2005**, *7*, 3297–3305.
- (54) Haruta, M.; Yamada, N.; Kobayashi, T.; Iijima, S. Gold Catalysts Prepared by Coprecipitation for Low-Temperature Oxidation of Hydrogen and of Carbon-Monoxide. *J. Catal.* **1989**, *115*, 301–309.
- (55) Visco, A. M.; Neri, F.; Neri, G.; Donato, A.; Milone, C.; Galvagno, S. X-Ray Photoelectron Spectroscopy of Au/Fe₂O₃ Catalysts. *Phys. Chem. Chem. Phys.* **1999**, *1*, 2869–2873.
- (56) Kishi, K.; Ikeda, S. X-ray Photoelectron Spectroscopic Study of Reaction of Evaporated Metal-Films with Chlorine Gas. *J. Phys. Chem.* A **1974**, 78, 107–112.
- (57) McNeillie, A.; Brown, D. H.; Smith, W. E.; Gibson, M.; Watson, L. X-Ray Photoelectron-Spectra of Some Gold Compounds. *J. Chem. Soc., Dalton Trans.* **1980**, 767–770.
- (58) Chen, Y. Q.; Tian, X. Z.; Zeng, W.; Zhu, X. P.; Hu, H. L.; Duan, H. G. Vapor-Phase Preparation of Gold Nanocrystals by Chloroauric Acid Pyrolysis. *J. Colloid Interface Sci.* **2015**, 439, 21–27.
- (59) Yang, S.; Park, K.; Kim, B.; Kang, T. Low-Temperature Vapor-Phase Synthesis of Single-Crystalline Gold Nanostructures: Toward Exceptional Electrocatalytic Activity for Methanol Oxidation Reaction. *Nanomaterials* **2019**, *9*, 595.
- (60) Nalbandian, L.; Papatheodorou, G. N. Raman-Spectra and Molecular Vibrations of Au₂Cl₆ and AuAlCl₆. Vib. Spectrosc. **1992**, 4, 25–34, DOI: 10.1016/0924-2031(92)87010-D.
- (61) Lu, J.; Crisci, G.; Niu, T.; Jacobson, A. J. A Polymeric Structure Containing Cu_2Cl_2 Units Bridged by 4,4'-Bipyridine: $(\text{PPh}_3)_2\text{Cu}_2(\mu\text{-Cl})_2(\mu\text{-4},4'\text{-bipyridine})$. *Inorg. Chem.* **1997**, 36 (22), 5140–5141, DOI: 10.1021/ic9705507.
- (62) Wong, C. H.; Schomaker, V. An Electron Diffraction Investigation of the Structure of Cuprous Chloride Trimer. *J. Phys. Chem. A* **1957**, *61*, 358–360.
- (63) Vihervaara, A.; Hatanpää, T.; Mizohata, K.; Chundak, M.; Popov, G.; Ritala, M. A Low-Temperature Thermal ALD Process for Nickel Utilizing Dichlorobis(Triethylphosphine)Nickel(II) and 1,4-Bis(Trimethylgermyl)-1,4-Dihydropyrazine. *Dalton Trans.* **2022**, *51*, 10898–10908.